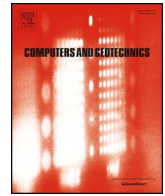




ELSEVIER

Contents lists available at ScienceDirect

## Computers and Geotechnics

journal homepage: [www.elsevier.com/locate/compgeo](http://www.elsevier.com/locate/compgeo)

## Research Paper

## A comprehensive parametric study of LBM-DEM for immersed granular flows

G.C. Yang<sup>a</sup>, L. Jing<sup>a,1</sup>, C.Y. Kwok<sup>a,\*</sup>, Y.D. Sobral<sup>b</sup><sup>a</sup> Department of Civil Engineering, The University of Hong Kong, Haking Wong Building, Pokfulam Road, Hong Kong<sup>b</sup> Departamento de Matemática, Universidade de Brasília, Campus Universitário Darcy Ribeiro, 70910-900 Brasília, DF, Brazil

## ARTICLE INFO

## Keywords:

LBM-DEM

Immersed moving boundary

Fluid-particle interaction

Granular collapse

## ABSTRACT

This paper presents a parametric study of a fluid-particle model which couples Lattice Boltzmann Method (LBM) and Discrete Element Method (DEM) using an immersed moving boundary technique. Benchmark cases with increasing complexity are simulated to understand the numerical accuracy, stability and efficiency of the algorithm. A guideline for a high-quality LBM-DEM model is proposed and applied to a test case of granular collapse in water. The simulation result shows excellent agreement with a companion experiment, which demonstrates the capability of LBM-DEM to describe the dynamics of densely packed and friction dominant immersed granular flows, highlighting its potential to study geophysical mass movements.

## 1. Introduction

For large-scale geophysical flows, such as debris flows and submarine landslides, runout distance is one of the key parameters for risk assessment and design of hazard mitigation works. Such catastrophic events usually involve fast transport of densely packed granular materials in a viscous fluid. However, there is still a concern about the accuracy of predictive models for immersed granular flows, especially when complex fluid-particle interactions play a non-negligible role in the dynamics of the flow. For example, the generation of excess pore fluid pressure may lead to fast or slow dynamics of saturated soils sliding down a slope [1]. The strong coupling effect between fluids and particles has a vital role underlying these micro-behaviors. Benefiting from highly advanced computer technology, numerical simulations have become appealing tools to study fluid-particle interaction problems, which require an accurate description of momentum exchange at the fluid-particle interface, together with an adequate resolution to account for the fully resolved pore-scale fluid flows.

Classic laws governing fluid-particle interactions have been developed and verified a long time ago based on massive physical experiments and rigorous theoretical analysis, such as the well-known Darcy's law [2] and the Ergun equation [3,4]. These semi-empirical relations usually serve as the underlying assumptions for successful multiphase numerical simulations, such as the coupling between Computational Fluid Dynamics (CFD) and Discrete Element Method (DEM) [5]. In this

kind of CFD-DEM technique, a fluid cell always has a size larger than the particles, resulting in an averaged porosity that is coupled to the fluid dynamics and to the resultant hydrodynamic forces. The coupling method with fluid cells larger than particles is denoted as the coarse-grid method in this work. Although the coarse-grid method has been successfully applied for a variety of problems [5–8], it can only provide limited pore-scale information. Therefore, fine-grid CFD-DEM method, in which one particle covers multiple fluid cells, has also been developed via the Immersed Boundary Method [9–11] to achieve a more general and accurate description of fluid-particle interaction, instead of heavily relying on the semi-empirical drag models. However, the fine-grid CFD-DEM method is sometimes numerically prohibitive due to its high computational cost to handle mesh generation (particularly, if dynamic local mesh refinement is used) together with the solution to the nonlinear Navier-Stokes equations, even for a small system involving several hundreds of particles [11].

Alternatively, the Lattice Boltzmann Method (LBM) can be coupled with DEM, in place of the conventional CFD, for the simulation of fluid-particle interaction problems. LBM solves the Boltzmann equation, which can be seen as an approximation of the incompressible Navier-Stokes equations, on a lattice at the mesoscopic scale based on kinetic theory [12–14]. When LBM is coupled with DEM, it shares the advantages of the fine-grid CFD-DEM method, such as the fully resolved pore-scale fluid flows and explicit calculation of hydrodynamic forces, and it is more efficient than CFD-DEM, benefiting from the much

\* Corresponding author.

E-mail address: [fkwok8@hku.hk](mailto:fkwok8@hku.hk) (C.Y. Kwok).<sup>1</sup> Current address: Department of Chemical and Biological Engineering, Northwestern University, Evanston, IL 60208, USA.

simplified governing equations with an excellent parallel computing performance [13]. Since LBM uses an explicit algorithm to stream fluid particles, it is also easier to couple the fluid flow with solid particles. As a result, reasonably large-scale problems can be simulated accurately and efficiently using the LBM-DEM technique.

For the coupling between LBM and DEM, there are two commonly used approaches, namely, the Momentum Exchange (ME) method [15,16] and the Immersed Moving Boundary (IMB) method [17,18]. Conceptually, the ME and IMB methods share the same basic idea of enforcing a no-slip boundary condition between fluids and solids with a hydrodynamic interaction according to the conservation law of momentum. In the ME method, the no-slip boundary condition is achieved via a bounce-back scheme at the fluid-particle interface [15], whereas, in the IMB method, the LBM collision operator is modified by following the non-equilibrium bounce-back principle if a fluid cell is covered by solids [17]. Several studies in the literature aimed at directly comparing the ME and IMB methods [19,20]. In our work, the IMB method is chosen to couple LBM with DEM, because it has a better sub-grid scale (SGS) resolution, and therefore, fewer distortions on the geometrical representation of the moving particles and on the hydrodynamic forces acting on them as particles move across fluid cells. It is also worth mentioning that we are aware that improvements of the ME method have been developed by introducing a more sophisticated interpolated bounce-back scheme [20] to improve its overall accuracy. However, the interpolation requires access to additional information at the neighboring fluid cells. As a result, the locality of the LBM calculation is lost and numerical issues may occur when particles are in close vicinity [20].

Successful two-dimensional (2D) and three-dimensional (3D) applications of the coupled LBM-DEM model via an IMB technique have been reported across multiple disciplines [19–30]. Han and Cundall [19] carried out a 2D investigation on the accuracy and efficiency of the IMB coupling method and concluded that a spatial resolution of 10 fluid cells per particle diameter provided an accurate description of fluid-particle interactions. Later, Rettinger and Rude [20] simulated a single particle settling in an ambient fluid in a 3D configuration and reported that a higher spatial resolution was required so that the particle velocity error was below 5%. The 3D scheme was also validated by Strack and Cook [24], in particular the phenomenon of two particles drafting, kissing, and tumbling in a fluid column was well captured. Then, the LBM-DEM model was further extended for particle transport in turbulent flows [22,23,25]. To improve the computational efficiency for 3D problems involving multiple particles, a relatively inexpensive lattice structure and a dynamic sub-cycling scheme were proposed by Owen et al. [26] and settling of a granular assembly in a viscous fluid field was successfully simulated. Recently, Wang et al. [29,30] implemented the bonded particle model into the contact law of DEM to study soil erosion in granular filters.

Unlike the abovementioned particle suspensions and bonded particle problems, this work is dedicated to the validation and application of the LBM-IMB-DEM approach in problems involving densely packed particles, whose motion is governed by both fluid-particle (viscous drag and lubrication) and particle-particle (collision and friction) interactions. These problems are quite common in nature and in geotechnical engineering and two unique features can be identified. First, the pore fluid flows must be resolved as accurately as possible due to the significant influence of excess pore fluid pressure on the flow dynamics [1,31]. In this regard, the LBM-DEM model must be formulated in 3D and a coarse-grid discrete particle simulation model may not be applicable [32]. Second, the shear between closely packed particles implies that the lubrication effects must be resolved with adequate accuracy [33]. An artificial lubrication model must be incorporated into the ME method due to the sudden loss of fluid when the gap between particles is less than one fluid cell [15,34]. The question whether the SGS resolution of the IMB method is sufficient to resolve the lubrication force remains to be answered.

The goal of this study is to apply the LBM-DEM method to simulate immersed granular flows in which solid particles are densely packed and the inter-particle friction plays a significant role. In order to examine various sources of errors, a series of benchmark cases following the strategy of increasing complexity are simulated, starting from a single stationary particle to multiple moving particles. After addressing the numerical issues, an application to the slumping of an immersed granular column initially at rest onto a horizontal plane is presented. The immersed granular collapse case has been widely applied in the literature to study the transient dynamics of large-scale geophysical mass movements due to its simple configuration but rich dynamics [8,31,33,35,36].

The rest of this paper is organized as follows. Section 2 introduces the numerical method, followed by the coupling scheme. Four benchmark cases are studied in Section 3 to test the performance of the LBM-DEM model in terms of accuracy, stability and efficiency. Section 4 presents numerical results of the immersed granular collapse simulation, together with the comparison to our experimental data. Section 5 summarizes the contributions of this work.

## 2. LBM-DEM formulation

### 2.1. Lattice Boltzmann method

LBM solves the hydrodynamics based on the kinetic theory at a mesoscopic scale [13]. The whole fluid system is described by a collection of fluid particles residing on a regular Cartesian mesh (lattice) with cubic cells. The number of fluid particles at each lattice node is quantified by a set of particle distribution functions (PDFs) with pre-defined discrete directions pointing to the neighboring lattice nodes. The PDF at time  $t$  positioned at  $\mathbf{x}$  pointing to the  $i$ -th direction is denoted as  $f_i(\mathbf{x}, t)$ . In this study, a D3Q19 lattice structure [12], as shown in Fig. 1(a), is used for 3D LBM simulations. The lattice uses 19 discrete velocities, instead of 15 or 27, to achieve a good balance between accuracy and efficiency [37]. The definitions of lattice direction, lattice node, lattice cell and lattice spacing ( $\delta_x$ ) are illustrated in Fig. 1(b).

In contrast to the conventional CFD that solves the nonlinear partial differential equations in terms of macroscopic variables, such as the fluid density  $\rho_f$  and the fluid velocity  $\mathbf{u}_f$ , the governing equation in LBM describes the evolution of PDFs. With a BGK approximation (named after Bhatnagar, Gross, and Krook [38]), the governing equation is written as:

$$f_i(\mathbf{x} + \mathbf{c}_i\delta_t, t + \delta_t) - f_i(\mathbf{x}, t) = -\frac{1}{\tau}[f_i(\mathbf{x}, t) - f_i^{eq}(\mathbf{x}, t)]. \quad (1)$$

The left-hand side (LHS) of Eq. (1) is the *streaming* process, during which the PDFs are passed to the neighboring lattice nodes (from  $\mathbf{x}$  to  $\mathbf{x} + \mathbf{c}_i\delta_t$ ) with a lattice velocity  $\mathbf{c}_i$  along the  $i$ -th direction over a LBM time step  $\delta_t$ . The right-hand side (RHS) of Eq. (1) is the *collision* process, during which the PDFs are linearly relaxed towards the equilibrium distribution functions (EDFs),  $f_i^{eq}(\mathbf{x}, t)$ , with a single dimensionless relaxation time  $\tau$ . The EDF adopted here is the Maxwellian one, which can be expanded into a Taylor series with respect to the macroscopic fluid velocity  $\mathbf{u}_f$ , as [39]:

$$f_i^{eq} = w_i\rho_f \left[ 1 + \frac{\mathbf{c}_i \cdot \mathbf{u}_f}{c_s^2} + \frac{(\mathbf{c}_i \cdot \mathbf{u}_f)^2}{2c_s^4} - \frac{u_f^2}{2c_s^2} \right], \quad (2)$$

where  $w_i$  is the weight associated with the lattice velocity  $\mathbf{c}_i$ , whose values are summarized in Table 1 and  $u_f = |\mathbf{u}_f|$ . The speed of sound  $c_s$  for D3Q19 is  $1/\sqrt{3}$  in lattice units [39]. The ratio between the magnitude of fluid velocity and the speed of sound is defined as the Mach number, i.e.,  $M = u_f/c_s$ .

Based on the fundamental laws of mass and momentum conservations, the macroscopic fluid density  $\rho_f$  and velocity  $\mathbf{u}_f$  can be reconstructed from the zeroth-order and first-order velocity moments of

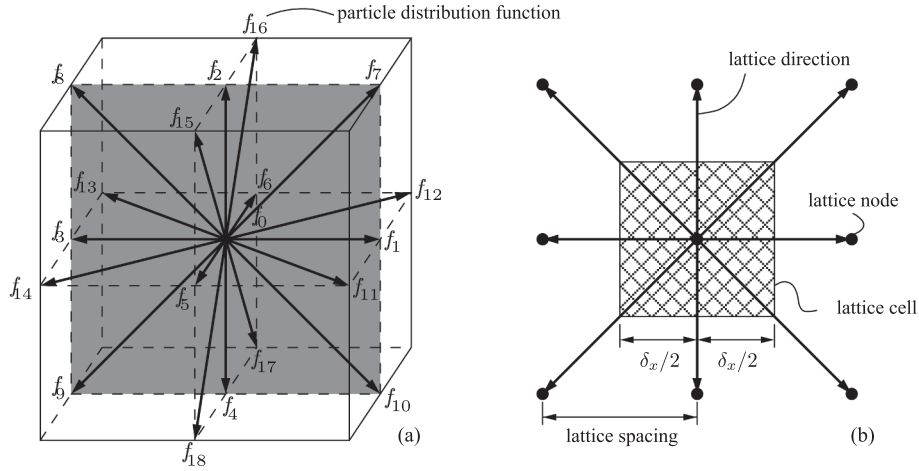


Fig. 1. (a) A D3Q19 lattice structure for 3D LBM simulations with 19 lattice velocities. Each lattice velocity is associated with a PDF from  $f_0$  to  $f_{18}$ ; the shaded plane is redrawn in (b) showing the lattice direction, lattice node, lattice spacing and a two-dimensional projection of a cubic lattice cell.

Table 1

Summary of the weight  $w_i$  for PDF  $f_i$  with lattice velocity  $\mathbf{c}_i$ . Note that the summation of all the weights shall be equal to the unity.

PDFs, $f_i$	Lattice velocity, $\mathbf{c}_i$	Weights, $w_i$
$f_0$	(0, 0, 0)	1/3
$f_1 - f_6$	( $\pm 1, 0, 0$ ), (0, $\pm 1, 0$ ), (0, 0, $\pm 1$ )	1/18
$f_7 - f_{18}$	( $\pm 1, \pm 1, 0$ ), ( $\pm 1, 0, \pm 1$ ), (0, $\pm 1, \pm 1$ )	1/36

the PDFs, as:

$$\rho_f = \sum_{i=0}^{18} f_i, \tag{3}$$

$$\rho_f \mathbf{u}_f = \sum_{i=0}^{18} \mathbf{c}_i f_i. \tag{4}$$

The Navier-Stokes equations can be recovered from Eq. (1) via a multi-scale (Chapman-Enskog) expansion [40], and a relationship between the relaxation time  $\tau$ , the LBM time step  $\delta_t$ , the lattice spacing  $\delta_x$  and the kinematic fluid viscosity  $\nu_f$  is obtained as:

$$\nu_f = c_s^2 \left( \tau - \frac{1}{2} \right) \frac{\delta_x^2}{\delta_t}. \tag{5}$$

In Eq. (5),  $c_s$  and  $\tau$  are model constants and  $\nu_f$  is a material property. The LBM time step  $\delta_t$  is dependent on the used discretization of the lattice grid with spacing  $\delta_x$ . The other macroscopic variable, pressure  $p$ , can be calculated from the fluid density by the equation of state [40]:

$$p = c_s^2 \rho_f. \tag{6}$$

The major source of compressibility error in LBM is the truncated Taylor expansion of the EDFs when the higher order terms of the Mach number are dropped off. To approximate an incompressible flow, it must fulfill  $M \ll 1$ . The incompressible requirement in LBM simulations poses a constraint on the LBM time step and thereby affecting the time step for the particle simulations. The synchronization between LBM and DEM will be addressed in Section 2.4.

### 2.2. Discrete element method

In many two-phase continuum simulations, such as fluidized beds, the interactions among solid particles is often approximately treated as an averaged lubrication force, and the motion of the solid particles are also averaged [41]. However, for the cases where the particles are densely packed and subjected to large displacements, such as the

immersed granular column collapse [8,33,36], the interaction between contacting particles has to be accurately calculated. A thoughtful choice is to adopt DEM [42] in order to better resolve the inter-particle interactions.

For the classic formulation of DEM, individual solid particles are taken as “rigid” bodies with “soft” contacts, allowing small overlaps between contacting objects. Fig. 2(a) shows a contact pair between particle  $a$  (in red) and particle  $b$  (in blue) with a overlap equal to  $\delta_n$ , which can be calculated by:

$$\delta_n = (r_a + r_b - r_{ab})\mathbf{n}, \tag{7}$$

where  $r_a$  and  $r_b$  are the radii of particle  $a$  and  $b$ , respectively. The spacing between the particle centers is denoted as  $r_{ab}$  and  $\mathbf{n}$  is the unit normal pointing to the particle center. For simplicity, all the particles in this study are spherical.

The contact forces can be calculated based on a simple spring-dashpot model [42], as shown in Fig. 2(b). The normal contact force  $\mathbf{F}_n$  is given by [42]:

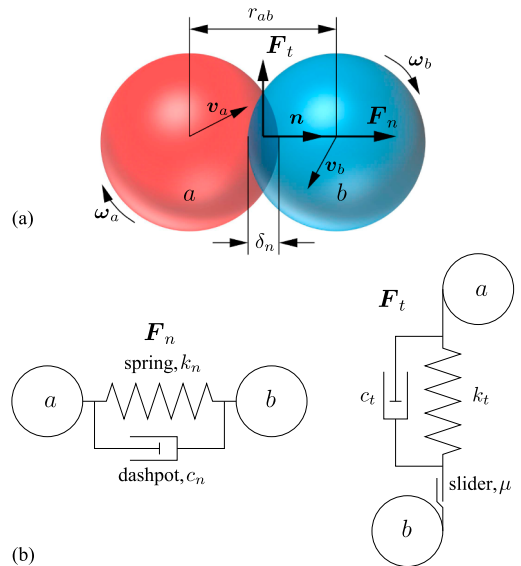


Fig. 2. (a) Sketch of two particles in contact: particle  $a$  in red and particle  $b$  in blue; (b) schematic sketches of the spring-dashpot model for the calculation of normal force  $\mathbf{F}_n$  and tangential force  $\mathbf{F}_t$ . (For interpretation of the references to colour in this figure legend, the reader is referred to the web version of this article.)

$$\mathbf{F}_n = k_n \delta_n + c_n \Delta \mathbf{u}_n, \quad (8)$$

where  $k_n$  and  $c_n$  are the stiffness and damping coefficient in the normal direction. The relative normal velocity is denoted as  $\Delta \mathbf{u}_n$ . The tangential contact force  $\mathbf{F}_t$  is written as [42]:

$$\mathbf{F}_t = -k_t \int_{t_{c,0}}^{t_c} \Delta \mathbf{u}_t dt - c_t \Delta \mathbf{u}_t, \quad (9)$$

where  $k_t$  and  $c_t$  are the stiffness and damping coefficient in the tangential direction and the relative tangential velocity is denoted as  $\Delta \mathbf{u}_t$ . The integral corresponds to an incremental spring that stores energy from the relative tangential motion, representing the elastic deformation of the particle surface over the contact duration from  $t_{c,0}$  to  $t_c$ . The tangential force points to a direction opposite to the tangential displacement. Besides, the magnitude of the tangential force is limited by the Coulomb friction  $\mu F_n$ , at which the two contacting particles start to slide against each other, where  $\mu$  is the smallest of the friction coefficients of the two particles in contact.

By changing  $k_n$ ,  $k_t$ ,  $c_n$  and  $c_t$  as a function of overlap and relative velocities, different contact models (or force-displacement laws) can be proposed for the calculation of contact force ( $\mathbf{F}_c = \mathbf{F}_n + \mathbf{F}_t$ ). In this study, the Hertz contact model is adopted [36,43]. Considering the forces (contact  $\mathbf{F}_c$ , gravity  $\mathbf{G}$ , fluid drag  $\mathbf{F}_f$ ) and torques (contact  $\mathbf{T}_c$ , fluid drag  $\mathbf{T}_f$ ) acting on a particle, its linear and angular velocities can be updated according to Newton's second law of motion:

$$m \mathbf{a} = \mathbf{F}_c + \mathbf{G} + \mathbf{F}_f, \quad (10)$$

$$I \dot{\boldsymbol{\omega}} = \mathbf{T}_c + \mathbf{T}_f, \quad (11)$$

where  $m$  and  $I$  are the mass and moment of inertia of the particle. The translational acceleration and angular velocity are denoted as  $\mathbf{a}$  and  $\boldsymbol{\omega}$ , respectively. The updated particle position and orientation can be calculated by taking the time integral of Eq. (10) and Eq. (11) via the Verlet method [44].

### 2.3. Immersed moving boundary method

In this study, the use of LBM and DEM for simulating the fluid and solid particle phases separately, necessitates an efficient and accurate coupling framework. Fig. 3(a) shows a two-dimensional sketch of two DEM spheres mapping on the LBM lattice grid. In this sketch, the lattice resolution,  $N$ , defined as the number of lattice cells per particle diameter, is equal to 5. The darkness of the lattice cell corresponds to its value of solid ratio ( $\varepsilon$ ), which is calculated as the volume of sub-cells fully covered by the solid particle divided by the total volume of a lattice cell; the colors white ( $\varepsilon = 0$ ), grey ( $0 < \varepsilon < 1$ ) and black ( $\varepsilon = 1$ ) refer to fluid, partially saturated and solid cells, respectively.

The basic principle of the IMB method is to introduce a new collision operator,  $\Omega$ , depending on the solid ratio,  $\varepsilon$ . Ideally, the exact value of  $\varepsilon$  can be found from a geometrical analysis, but it often requires high computational power. Therefore, a cell decomposition method is adopted [26], as illustrated in Fig. 3(b). In this method, the partially saturated cells are sub-divided into  $n_{sub}^3$  equal-sized sub-cells. An inside-outside algorithm is performed on the sub-cell centers and  $\varepsilon$  is estimated as the number of sub-cells inside the solid boundary (in black) divided by  $n_{sub}^3$ . Note that although the cell decomposition method is relatively easy for implementation, there are more efficient algorithms available by using polyhedral approximation [26] or Gaussian Quadrature [45].

For fluid cells with  $\varepsilon$  equal to 0, the normal hydrodynamic collision takes place, and  $\Omega$  is taken as the BGK collision operator,  $\Omega^f$ , as shown on the RHS of Eq. (1). For solid cells with  $\varepsilon$  equal to 1, a collision operator proposed by Noble and Torczynski [17] and based on the concept of non-equilibrium bounce-back [46] is applied and denoted as  $\Omega^s$ , which is given by:

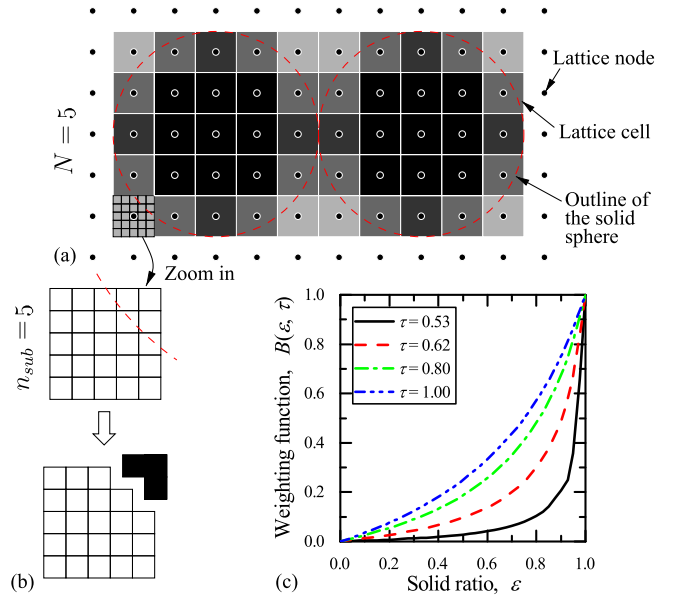


Fig. 3. (a) Two-dimensional sketch of two DEM spheres mapping on the LBM lattice grid with the lattice resolution  $N = 5$ . The darkness of a lattice cell corresponds to its solid ratio  $\varepsilon$ : white ( $\varepsilon = 0$ ), grey ( $0 < \varepsilon < 1$ ) and black ( $\varepsilon = 1$ ) refer to fluid, partially saturated and solid cells, respectively; (b) one of the partially saturated cells is zoomed in and its solid ratio  $\varepsilon$  is calculated via a cell decomposition method with 5 sub-slices; (c) plot of the weighting function  $B$  against the solid ratio  $\varepsilon$  at various relaxation times  $\tau$ .

$$\Omega_i^s = f_{-i}(\mathbf{x}, t) - f_{-i}^{eq}(\rho_f, \mathbf{u}_f) + f_i^{eq}(\rho_f, \mathbf{u}_s) - f_i(\mathbf{x}, t), \quad (12)$$

where  $\mathbf{u}_s$  is the macroscopic velocity of solid at the position of the lattice node  $\mathbf{x}$ . The subscript  $-i$  denotes the opposite direction of  $i$ . The role of the solid collision operator  $\Omega^s$  is to ensure a no-slip boundary condition between the fluid phase and the solid phase by setting the PDF,  $f_i(\mathbf{x} + \mathbf{c}_i \delta_i, t + \delta_i)$ , equal to the EDF,  $f_i^{eq}(\rho_f, \mathbf{u}_s)$ , plus the bounce-back of the non-equilibrium part in the opposite direction,  $f_{-i}(\mathbf{x}, t) - f_{-i}^{eq}(\rho_f, \mathbf{u}_f)$ .

For partially saturated cells with  $\varepsilon$  between 0 and 1, a weighting function,  $B$ , is used so that it gives:

$$\Omega = B \Omega^s + (1 - B) \Omega^f. \quad (13)$$

Following Noble and Torczynski [17], the weighting function can be calculated as a function of the relaxation time  $\tau$  and the solid ratio  $\varepsilon$ :

$$B(\varepsilon, \tau) = \frac{\varepsilon(\tau - 1/2)}{(1 - \varepsilon) + (\tau - 1/2)}. \quad (14)$$

Fig. 3(c) shows the value of the weighting function  $B$  against the solid ratio  $\varepsilon$  at four different values of relaxation time:  $\tau = 0.53, 0.62, 0.8$  and  $1.0$ . It can be seen that  $B$  varies from 0.0 to 1.0 as  $\varepsilon$  varies from 0.0 to 1.0. The first term in Eq. (13),  $B \Omega^s$ , represents the amount of disturbance to the fluid field due to the presence of solid particles.

Therefore, the hydrodynamic force  $\mathbf{F}_f$  is the sum of the momentum transfer along all lattice directions at  $n$  lattice cells covered by the solid particle (solid and partially saturated lattice cells), which gives:

$$\mathbf{F}_f = \sum_{j=1}^n B_j \sum_{i=0}^{18} \Omega_i^s \mathbf{c}_i. \quad (15)$$

The hydrodynamic torque  $\mathbf{T}_f$  is the cross product of the force and the corresponding lever arm, which can be written as:

$$\mathbf{T}_f = \sum_{j=1}^n \left[ B_j (\mathbf{x}_j - \mathbf{x}_s) \times \sum_{i=0}^{18} \Omega_i^s \mathbf{c}_i \right], \quad (16)$$

where  $\mathbf{x}_s$  is the center of mass of the solid particle, and  $\mathbf{x}_j$  is the coordinates of the  $j$ -th lattice cell. The hydrodynamic force and torque

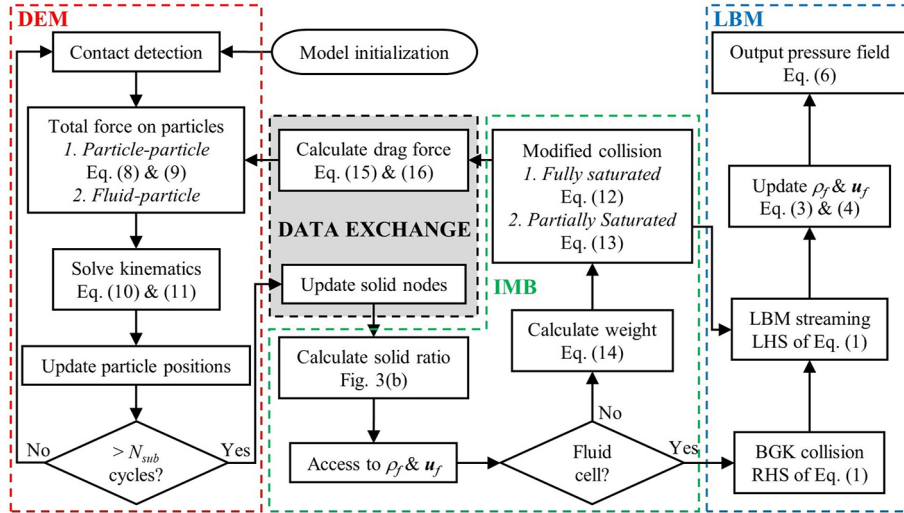


Fig. 4. Flowchart of the LBM-DEM coupling scheme.

calculated from Eq. (15) and Eq. (16) are back-substituted into Eq. (10) and Eq. (11) to update the kinematics and position of each individual solid particle.

#### 2.4. Coupling scheme

The LBM-DEM model is implemented by compiling an open source LBM C++ library (Palabos) as a master program, which calls a DEM code LIGGGHTS as an external library [47]. Fig. 4 shows the flowchart of the coupling scheme. The computing cycle starts with the generation of DEM particles and the initialization of the fluid field, followed by the particle-particle interactions via Eq. (8) and Eq. (9). To achieve a stable DEM simulation, the DEM time step,  $\Delta t$ , needs to be smaller than a critical value  $\Delta t_{cr}$  set by the stiffness and mass of the particles [48]. It is worth noting that the presence of fluid helps to damp the low-frequency elastic waves which can increase the stability of particle simulations, such that a  $\Delta t$  value greater than  $\Delta t_{cr}$  could be permissible. However, it is rather difficult to quantify this stabilization effect. Apart from this, the calculated critical DEM time step  $\Delta t_{cr}$  is in general smaller than the time step  $\delta_t$  in LBM simulations, especially for problems in geotechnical engineering due to the large stiffness of soils and rocks. To synchronize DEM with LBM,  $N_{sub}$  DEM sub-cycles are conducted for each step of LBM evolution, so it gives:

$$\Delta t = \frac{\delta_t}{N_{sub}}. \quad (17)$$

As a result, during the DEM sub-cycles, the hydrodynamic force  $\mathbf{F}_f$  and torque  $\mathbf{T}_f$  remain unchanged. It is not an easy task to pre-determine a proper value for  $N_{sub}$ , which itself is problem dependent. A  $N_{sub}$  value smaller than 10 is chosen in [27] for the pipe erosion problem. The influence of  $N_{sub}$  on the LBM-DEM results will be discussed in Section 3.2.

After  $N_{sub}$  of DEM sub-cycles, the updated particle positions are mapped on the lattice grid. Then, the lattice cells covered by the solid particles are identified. For partially saturated cells, the solid ratio  $\varepsilon$  is calculated via the cell decomposition method as shown in Fig. 3(b). According to the cell type (fluid, partially saturated or solid), the corresponding collision takes place. Note that the modified collision operator also appears in Eq. (15) and Eq. (16), therefore, the hydrodynamic force and torque are calculated right after the collision process (before streaming) for a high efficiency. Later, the hydrodynamic forces are passed back to the DEM module to resolve the particle motions. Then, the resulting PDFs stream to the neighboring lattice nodes. Based on the redistributed PDFs, the fluid density  $\rho_f$  and velocity  $\mathbf{u}_f$  can be

updated from Eq. (3) and Eq. (4). According to Eq. (6), the fluid pressure field can be calculated if required. Once these steps are completed, one cycle of LBM-DEM simulation is finished and the simulation carries on until the specified number of cycles is reached.

### 3. Model validation and parametric study

It is well recognized that an immersed granular collapse is a transient problem, involving isolated particles flowing in a fluid (front and granular free surface), fluid flowing through a static granular skeleton and particles shearing against each other. To examine various sources of numerical errors, the LBM-DEM model is first benchmarked against four cases in this section. The roles of the lattice resolution and the relaxation time are first investigated via a simple problem of Poiseuille flow past a fixed sphere in Section 3.1. Section 3.2 presents the simulation of a heavy particle settling in an ambient fluid to test the sub-cycling scheme and to examine the numerical error caused by particle moving across multiple fluid cells. The influences of lattice resolution and relaxation time on the numerical results are discussed again in this transient scenario regarding the particle settling velocity. Then, the LBM-DEM model for densely packed granular systems is validated by simulating a flow through a porous medium in Section 3.3. After that, the capability of describing the rheology of fluid-particle mixtures is highlighted in Section 3.4, in which a concentrated suspension in a planar Couette flow is simulated. The major objective of this section is to propose a guideline for a successful immersed granular collapse simulation in Section 4.

#### 3.1. Poiseuille flow past a fixed particle

##### 3.1.1. Problem description

The successful coupling between LBM and DEM is first tested against a simple benchmark case: a Poiseuille flow past a fixed solid particle, as shown in Fig. 5. The hydrodynamic force and torque acting on the particle at steady-state are measured and compared to the available analytical solutions [49]. From this simple benchmark case, the influences of two model parameters, i.e., the lattice resolution  $N$  and the relaxation time  $\tau$ , which play significant roles in LBM-DEM simulations, are discussed in detail. In addition, the least required lattice resolution and the recommendation for the relaxation time are provided.

As shown in Fig. 5, the fixed particle is positioned between two parallel solid walls with separation of  $l_y = 10$  mm. The radius of the particle is  $R = 1$  mm, which is positioned at half-way in  $x$  and  $z$

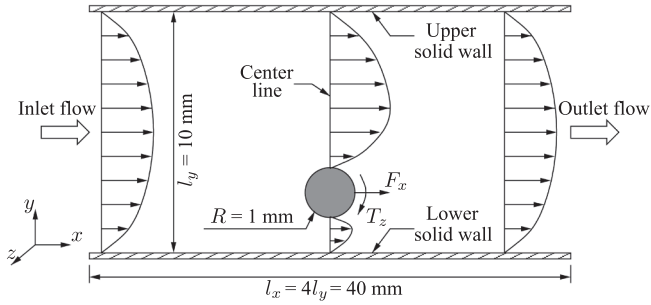


Fig. 5. 2D sketch of a Poiseuille flow past a fixed particle positioned at one-quarter of the distance between the two parallel solid walls.

directions and 2.5 mm away from the lower wall measured from the particle center. The upper and lower solid walls in  $y$ -direction are set to be no-slip boundary conditions, while periodic boundaries are applied in the other two directions. The lengths in  $x$  and  $z$  directions are large enough with  $l_x = l_z = 4l_y = 40$  mm to make sure that the reflected images of the particle are hydrodynamically decoupled [50]. The flow is driven from left to right by a body force with an equivalent pressure gradient equal to 2.5E-5 Pa/m. The fluid density ( $\rho_f$ ) and dynamic viscosity ( $\mu_f$ ) are set to be 1000 kg/m<sup>3</sup> and 0.001 Pa·s. The Reynolds number calculated from the mean flow velocity and the particle diameter is about 4.2E-7, which is small enough to achieve Stokes flow.

Approximate analytical solutions for the magnitudes of hydrodynamic force  $F_x$  and torque  $T_z$  acting on the particle caused by the drag from the fluid flow are available from Happel and Brenner [49], which are given by:

$$F_x = 6\pi\rho_f\nu_fRU \frac{1 - 1/9(R/l_y)^2}{1 - 0.6526(R/l_y) + 0.316(R/l_y)^3 - 0.242(R/l_y)^4}, \quad (18)$$

$$T_z = \frac{8}{3}\pi\rho_f\nu_fR^2U \frac{R}{l_y} \left[ 1 + 0.0758\left(\frac{R}{l_y}\right) + 0.049\left(\frac{R}{l_y}\right)^2 \right], \quad (19)$$

where  $U$  is the upstream mean flow velocity.

To compare with Happel and Brenner's estimation as shown in Eqs. (18) and (19), the relative error in percentage is defined as:

$$\% \text{ error} = \left( \frac{\text{Analytical solution} - \text{Numerical result}}{\text{Analytical solution}} \right) \times 100. \quad (20)$$

### 3.1.2. Effects of the lattice resolution

Similar to many other numerical methods, the accuracy of LBM-DEM simulations highly depends on the spatial (lattice) resolution. In this study, numerical simulations with the lattice resolution,  $N$ , defined as 5, 10, 20 and 25 are carried out. For each lattice resolution, the number of sub-slice  $n_{sub}$  varies between 2, 5 and 10 for the calculation of the solid ratio  $\varepsilon$ . The relative force and torque errors for different  $n_{sub}$  values are plotted against the lattice resolution in Fig. 6. For these simulations, the relaxation time is fixed at  $\tau = 1.0$ .

When the lattice resolution is low, with  $N = 5$ , the force and torque errors can be as high as 17.8% and 31.4%, when  $n_{sub} = 5$ . As  $N$  increases from 5 to 20, both the calculated hydrodynamic force and torque errors decrease rapidly. At  $N = 20$ , the LBM-DEM model is able to produce results within 4.5% of errors compared to Happel and Brenner's estimation. Further increase of lattice resolution from  $N = 20$  to  $N = 25$  only yields a minimal improvement in accuracy. Hence, a spatial resolution of at least 20 lattice cells across one particle diameter is recommended to achieve reasonably accurate coupled LBM-DEM simulations using the IMB method.

The fluid-like behavior of the partially saturated cells in the LBM-DEM model is determined by their solid ratios. And indeed, the accuracy of solid ratio calculation does affect the LBM-DEM results

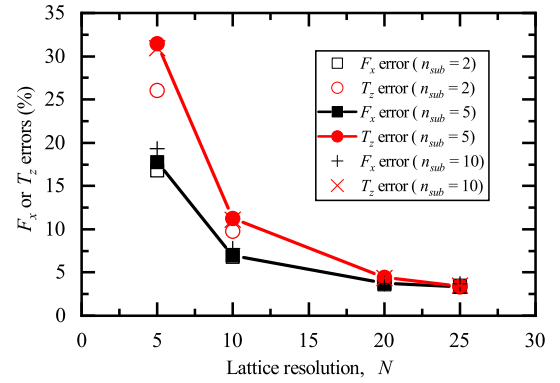


Fig. 6. Relative errors for the hydrodynamic force and torque against the lattice resolution  $N$  for simulations with various  $n_{sub}$  values. The results with  $n_{sub} = 5$  (filled symbols) are connected to show the convergence of the numerical results as  $N$  increases. The relaxation time is fixed at  $\tau = 1.0$ .

significantly when the lattice resolution is low. However, if the lattice resolution is sufficiently high, for example  $N = 20$ , the influence from  $n_{sub}$  is negligible. And it will also be shown in Section 3.1.4 that  $n_{sub}$ , within the range of consideration, is not the major factor affecting the computational time in this particular case.

### 3.1.3. Effects of the relaxation time

The relaxation time  $\tau$  physically determines how fast the PDFs recover the current EDFs, as shown in Eq. (1). Previous study has already revealed that the BGK (or single-relaxation-time) model adopted in our work may lead to inaccurate no-slip boundary locations [26,51–53]. To investigate the influence of the relaxation time  $\tau$  on the coupling between LBM and DEM quantitatively, numerical simulations with  $\tau$  equal to 0.53, 0.62, 0.8 and 1.0 are carried out with the fluid viscosity being unchanged. The relative force and torque errors are plotted against the relaxation time in Fig. 7 at a low ( $N = 5$ ) and a high ( $N = 20$ ) lattice resolution.

Interestingly, it can be seen that as  $\tau$  increases, both the relative force and torque errors increase roughly in a linear way. The dependence of the LBM-DEM results on the relaxation time is much more significant when the lattice resolution is low at  $N = 5$ . The relaxation time is able to affect the accuracy of the LBM-DEM model in several different ways.

First, for a constant fluid viscosity  $\nu_f$  and a fixed lattice spacing  $\delta_x$ , the LBM time step  $\delta_t$  decreases as the relaxation time  $\tau$  decreases according to Eq. (5). As a result, the hydrodynamic forces on particles can be updated more frequently. In addition, when the fluid velocity is normalized by the term  $\delta_x/\delta_t$ , the resultant fluid velocity in lattice units is also reduced. In this way, the Mach number drops as  $\tau$  decreases, resulting in smaller compressibility errors for the fluid solution. When

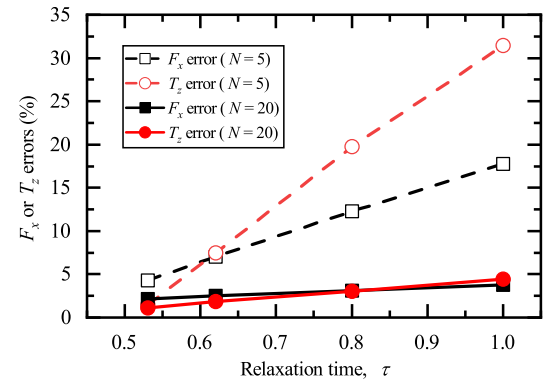
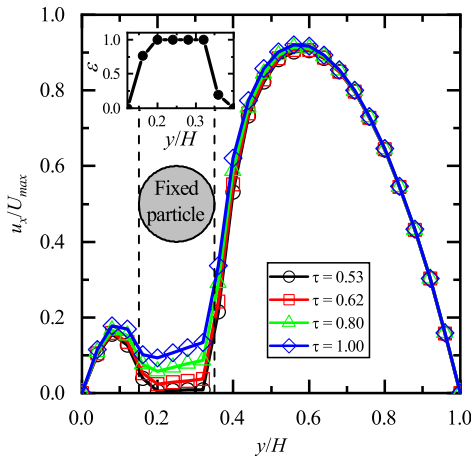


Fig. 7. Relative force and torque errors against the relaxation time  $\tau$  at lattice resolutions  $N = 5$  and  $N = 20$ .



**Fig. 8.** Profiles of the normalized streamwise velocity at the section in  $y$ -direction going through the center of the particle from LBM-DEM simulations with various relaxation times:  $\tau = 0.53, 0.62, 0.8$  and  $1.0$ . The lattice resolution is  $N = 5$ .

the fluid viscosity is small and the Reynolds number is high, an extremely small  $\tau$  value (but greater than 0.5) needs to be used so that the compressibility error is small enough. For example, a simplified laboratory model of vacuum dredging systems for mineral recovery was simulated by LBM-DEM and the relaxation time  $\tau$  was set to be 0.5002 [25]. In the case of soil erosion in granular filters, a  $\tau$  value as small as 0.5000005 was adopted [30,35].

When the fluid is coupled with the particles, the relaxation time has a significant influence on the no-slip boundary conditions [26,51–53]. In order to examine this issue, the streamwise velocity profiles at the center line, as shown in Fig. 5, are plotted in Fig. 8 for simulations with various relaxation times. The streamwise velocity  $u_x$  is normalized by the theoretical maximum flow velocity  $U_{max}$  in the absence of the particle. The inserted figure shows the distribution of the solid ratio.

As shown in Fig. 8, when  $\tau$  is large and close to 1.0, the fluid momentum is able to diffuse into the solid particle, producing non-zero flow velocities at the solid cells (with  $\varepsilon = 1$ ). As  $\tau$  decreases from 1.0 to 0.53, the flow velocities at the solid cells decrease to nearly zero values, indicating a highly improved no-slip boundary condition. As a result, the involved hydrodynamic interactions via momentum exchange between the fluid and the solid particle are also better described as  $\tau$  decreases. This result agrees with previous findings that the erroneous slip velocity increases with the relaxation time when the bounce-back boundary condition is applied [26,46]. Due to this diffusion effect of fluid momentum, the fluid field can only feel a transparent particle, resulting in the underestimated drag force especially when  $\tau$  is large, which agrees with the results in Fig. 7.

The relaxation time can also affect the LBM-DEM results via the weighting function  $B(\varepsilon, \tau)$ , as shown in Fig. 3(c). As the relaxation time  $\tau$  increases, the  $B$ - $\varepsilon$  curve shifts upwards, resulting in a more solid-like behavior for the partially saturated cells. However, the currently adopted weighting function is still not able to adequately compensate for the weakened fluid-particle interaction due to the diffusion effect. The relaxation time dependence can be alleviated by adopting a two-relaxation-time collision operator [52] or a modified weighting function [53]. According to our results, a super-linear relationship between  $B$  and  $\varepsilon$  can be proposed in future to potentially increase the accuracy of the LBM-DEM model when  $\tau$  increases.

### 3.1.4. Computational cost

The calculated hydrodynamic force and torque from several selected LBM-DEM simulations and the relative errors compared to Happel and Brenner's estimation [49] are listed in Table 2. All cases are simulated with two compute nodes, each of which is equipped with two 10-core

**Table 2**

Comparison between the LBM-DEM results and Happel and Brenner's estimation [49] in terms of the hydrodynamic force and torque acting on a fixed particle in Poiseuille flow. The analytical solutions for the hydrodynamic force and torque are 5.7628E-12 N and 8.1537E-16 N·m, respectively.

$N$	$n_{sub}$	$\tau$	$F_x$ (E-12 N)	$T_z$ (E-16 N·m)	Error $F_x$ (%)	Error $T_z$ (%)	$T$ (min)
5	5	1.0	4.7375	5.5904	17.7910	31.4374	0.58
10	5	1.0	5.3606	7.2359	6.9793	11.2560	8.53
20	5	1.0	5.5462	7.7928	3.7595	4.4260	182.52
25	5	1.0	5.5709	7.8732	3.3305	3.4398	482.77
20	2	1.0	5.5553	7.8202	3.6016	4.0905	184.05
20	4	1.0	5.5484	7.8001	3.7203	4.3372	173.90
20	10	1.0	5.5476	7.7986	3.7343	4.3546	180.15
20	5	0.8	5.5829	7.9051	3.1223	3.0488	296.75
20	5	0.62	5.6166	8.0031	2.5379	1.8471	721.40
20	5	0.53	5.6385	8.0608	2.1564	1.1390	4312.90

Intel Xeon E5-2600 v3 processors and 96 GB physical memory. The total simulation time,  $T$ , is presented at the last column of Table 2 in minutes. We can identify two parameters that play a major role in the computational demand, including the lattice resolution  $N$  and the relaxation time  $\tau$ . Generally speaking, the computational cost increases rapidly as  $N$  increases and  $\tau$  decreases. In return, the accuracy of the LBM-DEM model is usually improved.

## 3.2. Particle settling in an ambient fluid

### 3.2.1. Problem description

In order to test the sub-cycling scheme and the additional numerical error caused by particle moving across multiple lattice cells, the case of a single heavy particle settling in an ambient fluid is simulated, as shown in Fig. 9. The numerical test setup is the same as the physical experiment conducted in [34]. A particle with diameter  $d_p = 15$  mm is released at an initial height  $h_0 = 120$  mm in a container filled with fluid. The initial velocity is set to be zero. The container has a dimension of 100 mm, 160 mm, and 100 mm in  $x$ ,  $y$  and  $z$  directions, respectively. During the sedimentation of the particle, the settling velocity  $v$  and the distance to the bottom of the container  $h$  are recorded.

We have repeated the same experiments referenced in [34] with four different particle Reynolds numbers:  $Re = 1.5$  (E1), 4.1 (E2), 11.6 (E3) and 31.9 (E4), based on the terminal velocity of the particle in an infinite fluid field ( $v_{inf}$ ), by varying the fluid density and viscosity. The lattice resolution and the relaxation time are correspondingly set to be 20 and 0.56 for all four cases, which gives the LBM time steps equal to 2.93E-5 s, 5.12E-5 s, 9.58E-5 s and 1.86E-4 s for E1 to E4, respectively. The solid walls in all directions are set as no-slip boundary conditions using the bounce-back method [51].

### 3.2.2. Results and discussion

Fig. 10 shows the comparison between the calculated numerical results and the measured experimental data in terms of the particle trajectory and the evolution of settling velocity. It can be seen that for

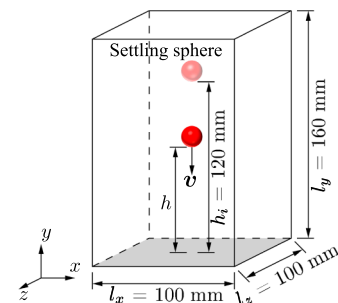


**Fig. 9.** Sketch of a single heavy particle settling in an ambient fluid.

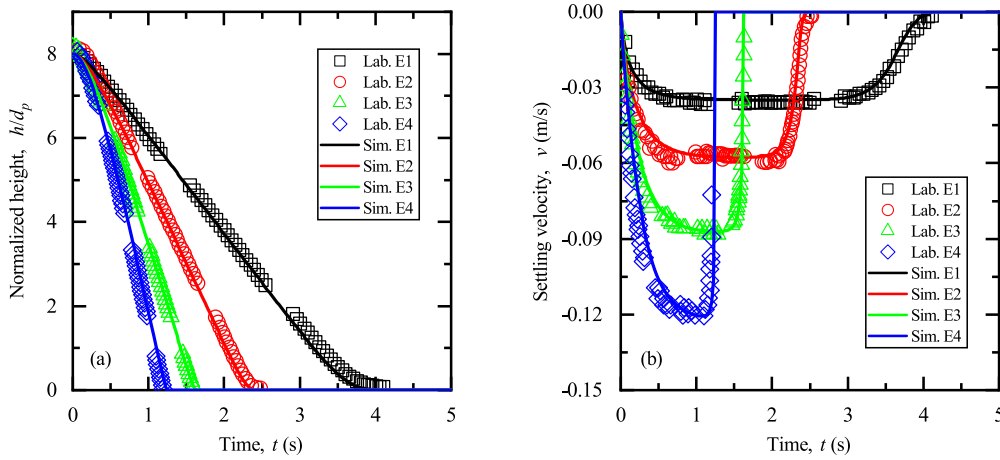


Fig. 10. Comparison between the simulated and measured results regarding to (a) the particle settling trajectory and (b) the particle settling velocity evolution. Four different cases are simulated, including E1 ( $Re = 1.5$ ), E2 ( $Re = 4.1$ ), E3 ( $Re = 11.6$ ) and E4 ( $Re = 31.9$ ). The lattice resolution and the relaxation time are set to be 20 and 0.56, respectively.

the case E1 with a low Reynolds number and high fluid viscosity, the settling velocity first increases until a maximum and constant value ( $v_{max}$ ) is reached, at which the weight of the particle is balanced by the buoyancy force and the drag force. After that, the particle velocity decreases slowly as it approaches the bottom solid wall due to the additional force produced by lubrication effects [54]. For the case E4 with a high Reynolds number and small fluid viscosity, the particle settles with a much higher acceleration and velocity, and then decelerates quickly. A settling period with stable terminal velocity is barely observed. All in all, the agreement between the numerical results and the experimental data serves as the evidence for the reliability of the presented coupling scheme for problems with moving particles in a viscous fluid.

In order to further confirm the influences of lattice resolution  $N$  and relaxation time  $\tau$  discussed in Section 3.1, we simulate the case E1 with different  $N$  and  $\tau$  values, and the particle settling velocity at near wall approach is presented in Fig. 11. When  $N$  is small or  $\tau$  is large, the repulsive lubrication force on the particle at bottom approach is under predicted (see Figs. 6 and 7). As a result, the flow is not well resolved and the particle stops abruptly. It is reported that this abrupt stop remains even if the lattice resolution is increased in the ME method [34]. An artificial lubrication force model can be incorporated into the ME method to improve the velocity decay [15,34]. However, it also brings in a problem that the sedimentation time extends further and becomes unrealistically long (the magnitude of lubrication force can be huge when the gap is small). In contrast, Fig. 11 clearly shows that a smooth velocity decay can be achieved if the IMB method is adopted with a high enough  $N$  and an adequately small  $\tau$ . Unlike the ME method, a

layer of fluid is solved by the partially saturated cells when  $h < \delta_x$ . The ability to solve fluid-particle interactions when solids move in close vicinity highlights the SGS resolution of the IMB method and makes LBM-DEM coupled by IMB an adequate numerical tool to simulate immersed dense shear flows (see Section 4).

The numerical convergence is assessed regarding the velocity ratio, which is defined as  $v_{max}/v_{inf}$ , as shown in the insets of Fig. 11. As  $N$  increases (above 20) and  $\tau$  decreases (below 0.56), a convergent velocity ratio can be achieved. Note that  $v_{max}$  in the LBM-DEM simulation turns out to be smaller than  $v_{inf}$  due to the hindrance from the side walls.

The case E1 is also simulated with different number of sub-cycles ( $N_{sub} = 1, 10, 100, 1000$ ) and the evolution of particle settling velocity is plotted in Fig. 12(a).  $N$  and  $\tau$  are fixed to be 20 and 0.56, respectively.  $N_{sub} = 1$  means that every cycle of LBM simulation is accompanied with one cycle of DEM calculation. In our coupling scheme, the LBM time step  $\delta_t$  is first determined based on the predefined lattice resolution, relaxation time and fluid viscosity, see Eq. (5). The increase in  $N_{sub}$  only reduces the DEM time step  $\Delta t$  for a better DEM stability. In other words, the frequency of momentum exchange between the fluid and the solid particle remain unchanged in terms of physical time (independent on  $N_{sub}$ ). Therefore, when  $N_{sub} = 1$ ,  $\Delta t$  is too large that the solid particle moves more than it should within one DEM time step. Consequently, the solid particle settles quickly with a maximum velocity almost twice of the accurate value, as shown in Fig. 12(a). The problem can be well addressed by increasing  $N_{sub}$ . And there is no observable difference between the cases with  $N_{sub} = 100$  and  $N_{sub} = 1000$ , indicating that a stable DEM solution is obtained. Besides, Fig. 12(b) shows little

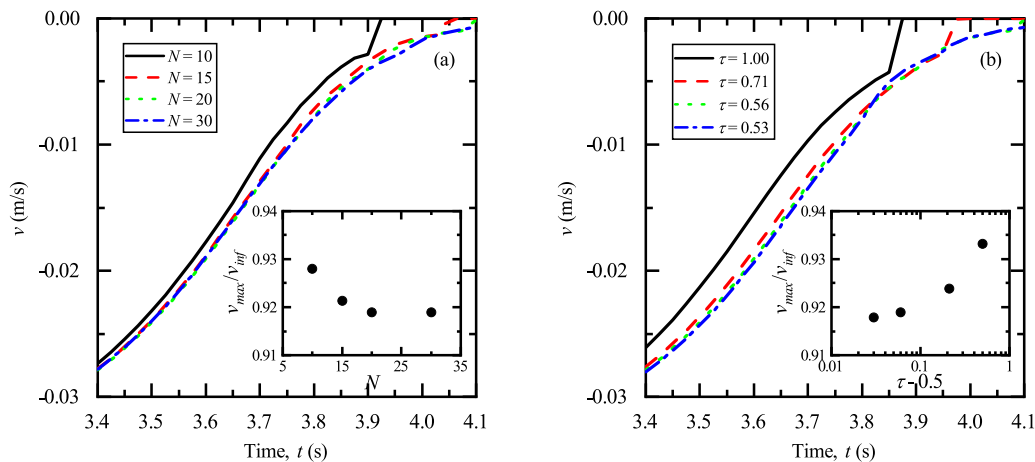
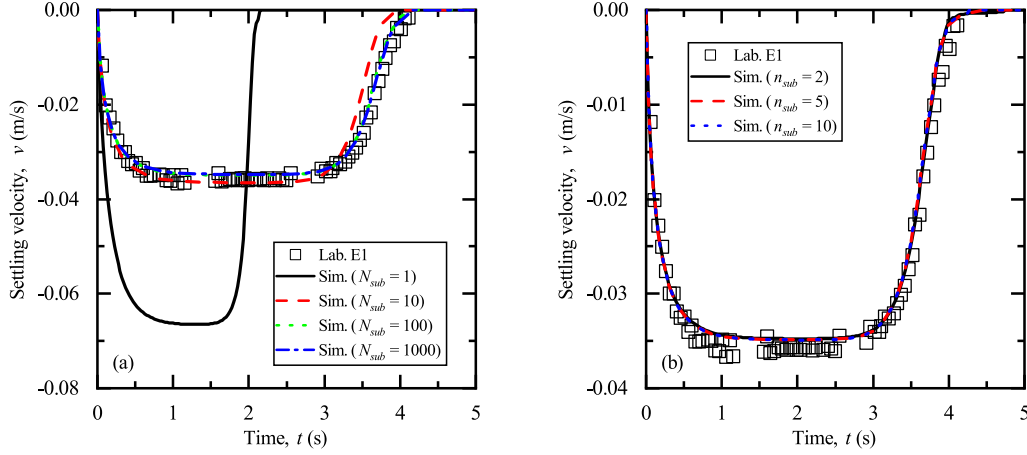


Fig. 11. Particle settling velocity  $v$  at near wall approach in the case E1 affected by (a) the lattice resolution  $N$  ( $\tau$  is fixed to be 0.56) and (b) the relaxation time  $\tau$  ( $N$  is fixed to be 20). The insets show the influences of  $N$  and  $\tau$  on the velocity ratio  $v_{max}/v_{inf}$ .



**Fig. 12.** Influences of (a) the number of sub-cycles  $N_{sub}$ ; and (b) the number of sub-cells  $n_{sub}$  on the time evolution of particle settling velocity  $v$  in the case E1.  $N$  and  $\tau$  are fixed to be 20 and 0.56, respectively, so they give a constant LBM time step  $\delta_t = 2.93E-5$  s.

influence of the number of sub-cells  $n_{sub}$  on the particle settling velocity, which agrees with our observation in Section 3.1.

### 3.3. Flow through densely packed particles

#### 3.3.1. Problem description

In order to examine the accuracy of the LBM-DEM model in problems involving multiple solid particles, a flow through a densely packed granular medium is simulated, as shown in Fig. 13. The granular medium consists of monodispersed particles with diameter  $d_p = 1$  mm packed in a simple cubic arrangement. The fluid has a density  $\rho_f = 1000$  kg/m<sup>3</sup> and a dynamic viscosity  $\mu_f = 0.001$  Pa·s. The granular medium has a dimension of  $10d_p$ ,  $5d_p$  and  $5d_p$  in  $x$ ,  $y$  and  $z$  directions, respectively. An additional one  $d_p$  of spacing is left at the inlet and outlet for the development of inflow and outflow. Periodic boundaries are defined in all directions. The flow is driven from left to right by seven different pressure differences ( $\Delta P$ ), including 1 Pa, 5 Pa, 10 Pa, 20 Pa, 50 Pa, 100 Pa and 200 Pa. Again, the lattice resolution is set to be  $N = 20$ . As  $\Delta P$  increases, the fluid velocity also increases, therefore a smaller relaxation time is required to reduce the compressibility error. In order to keep the maximum fluid density variation below 1%, the relaxation time is gradually reduced by following the order of 0.58, 0.53, 0.524, 0.516, 0.51, 0.508 and 0.505 with the increase of  $\Delta P$ . All simulations last for 5 s, which is long enough to allow the flow to be fully developed.

The total pressure loss can be described by the well-known Ergun equation [3] which is composed of two terms: a viscous loss proportional to the fluid velocity and an inertial loss proportional to the square of the fluid velocity, given by:

$$\frac{\Delta P}{L} = \frac{150\mu_f(1-\phi_f)^2}{d_p^2\phi_f^3}U + \frac{1.75\rho_f(1-\phi_f)}{d_p\phi_f^3}U^2, \quad (21)$$

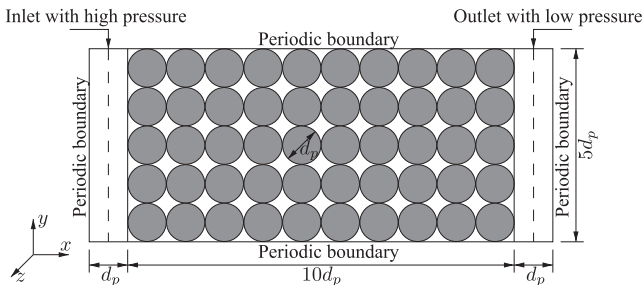


**Fig. 13.** Numerical setup of flow through densely packed particles in a cubic arrangement.

where  $L$  is the length of the granular medium and equal to  $10d_p$ . The porosity is denoted as  $\phi_f$  and equal to 0.4764. The superficial fluid velocity is denoted as  $U$ .

Following Niven [55], Eq. (21) can be rewritten in the form of:

$$f^* = \frac{\Delta P}{L} \frac{d_p}{\rho_f U^2 (1-\phi_f)} = \frac{150}{\text{Re}_p^*} + 1.75, \quad (22)$$

where  $f^*$  is known as the packed bed friction factor.  $\text{Re}_p^*$  is a modified particle Reynolds number based on the interstitial fluid velocity, which is given by:

$$\text{Re}_p^* = \frac{\rho_f d_p U}{\mu_f (1-\phi_f)}. \quad (23)$$

#### 3.3.2. Results and discussion

LBM-DEM simulations are conducted, and the resultant friction factor  $f^*$  is plotted against the modified particle Reynolds number  $\text{Re}_p^*$  in Fig. 14, together with the empirical Ergun equation, i.e. Eq. (22). Han and Cundall [28] verified their LBM-DEM model against the Ergun equation based on a different configuration. Instead of simulating a flow through densely packed particles, a single particle was extracted from a porous medium and simulated with periodic boundaries defined in all directions. The result from a periodic particle model is also plotted in Fig. 14 for comparison. It can be seen that both the porous medium model and the periodic particle model can well predict the friction factor  $f^*$  over a wide range of Reynolds number  $\text{Re}_p^*$ . It is quite encouraging based on the fact that the LBM-DEM model only resolves the

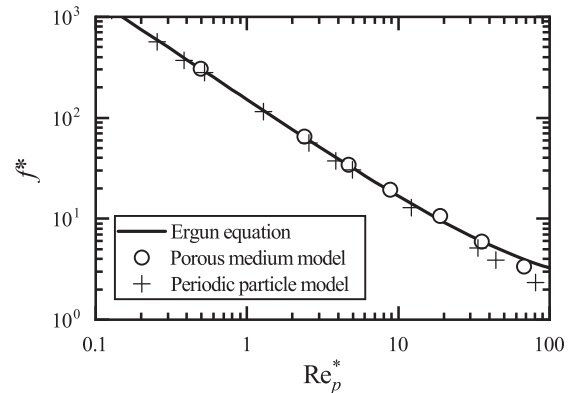


**Fig. 14.** Comparison between the LBM-DEM results and the Ergun equation in terms of the packed bed friction factor  $f^*$  at various modified particle Reynolds numbers  $\text{Re}_p^*$ .

local fluid-particle interactions at the pore-scale, while the Ergun equation describes the overall resistance on the fluid field from the whole porous structure. In other words, the macroscopic behavior is automatically recovered from the microscopic fluid-particle interactions.

The porous medium model in this study is found to yield better accuracy compared to the periodic particle model when  $Re_p^*$  is greater than 40. However, both LBM-DEM simulations tend to underestimate the friction factor  $f^*$  at high  $Re_p^*$ . It is probably due to the unresolved turbulence when the fluid inertia becomes significant. One solution is to further increase the lattice resolution  $N$  so that more eddies can be resolved adequately well [20]. However, the increase in  $N$  could make the LBM-DEM simulation computationally prohibitive (see Section 3.1.4). Alternatively, a turbulence model can be incorporated into LBM to capture the effects from unresolved small eddies without sacrificing the efficiency [14,23,25,56]. For the purpose of simulating the granular collapse in Section 4, the incorporation of a turbulence model yields little influence on the overall collapse behavior. For high-Re flows, such as fluidized beds, using the turbulence model could potentially improve the accuracy without significantly increasing the computational cost.

Different from the previous two cases, which involve only one single particle, the whole fluid field is covered by a much larger percentage of partially saturated and solid cells in the flow through a porous medium. Simulations with  $n_{sub} = 2, 5$  and 10 have been carried out. Again, the accuracy is barely affected when a lattice resolution as high as  $N = 20$  is adopted. Nevertheless, the computational time increases by 15% and 38% as  $n_{sub}$  increases from 2 to 5 and 10, respectively.

### 3.4. Couette flow of particle suspensions

#### 3.4.1. Problem description

In an immersed granular collapse, the dynamics of the fluid-particle mixture is governed by particle-particle interactions either by direct contact or via the interstitial fluid. To highlight the capability of the proposed LBM-DEM model in capturing the complex fluid-particle interactions, a problem involving multiple and movable particles submerged in a fluid is simulated. Fig. 15 shows a concentrated suspension of neutrally buoyant and monodispersed particles with diameter  $d_p = 1$  mm. The fluid density and dynamic viscosity are set to be  $\rho_f = 1000$  kg/m<sup>3</sup> and  $\mu_f = 0.001$  Pa·s, respectively. The simulation domain has a size equal to  $10d_p, 10d_p$  and  $5d_p$  in the  $x, y$ , and  $z$  directions, respectively. The flow is driven by moving the top and bottom solid walls to the right and to the left with a constant velocity  $u_w = 0.001$  m/s. Periodic boundaries are defined in the  $x$  and  $z$

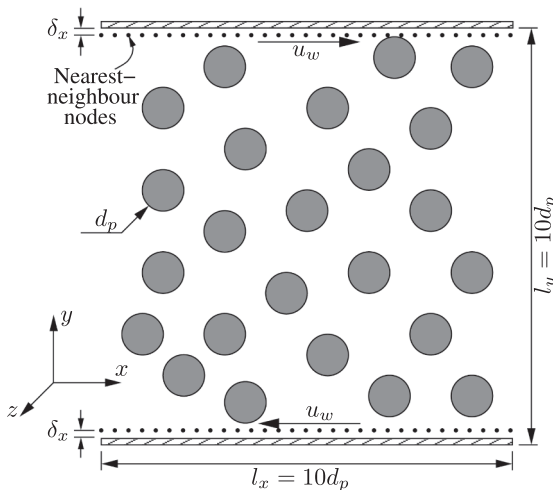


Fig. 15. 2D sketch of a concentrated suspension undergoing planar Couette flow.

directions. In this way, an average shear rate,  $\dot{\gamma}$ , in the fluid can be calculated, as:

$$\dot{\gamma} = \frac{2u_w}{H}, \quad (24)$$

where  $H$  is the distance between the two parallel solid walls. The wall shear stress,  $\tau_w$ , is given by:

$$\tau_w = \mu_f \dot{\gamma}. \quad (25)$$

Eq. (25) is usually applied to measure the fluid viscosity via rheometers. And for a pure Newtonian fluid,  $\mu_f$  remains constant, independent on the magnitude of shear rate. However, if there are particles suspended in the fluid, the rheology of the mixture becomes different from that of the pure fluid. Generally speaking, the apparent viscosity of the particle suspension  $\mu_f^*$  increases as the solid volume fraction  $\phi_p$  increases. The relationship between  $\mu_f^*$  and  $\phi_p$  was first described by Einstein [57], written as:

$$\mu_f^*(\phi_p) = \mu_f(1 + 2.5\phi_p). \quad (26)$$

Einstein's viscosity equation is deduced with the assumption of negligible interactions among solid particles. Therefore, Eq. (26) is only valid for extremely dilute systems. Following Einstein, researchers have spent huge efforts trying to extend Einstein's viscosity equation to suspensions with finite concentrations. According to the classic work from Mooney [57], the apparent viscosity of a suspension of monodispersed particles is:

$$\mu_f^*(\phi_p) = \mu_f \exp\left(\frac{2.5\phi_p}{1 - k\phi_p}\right), \quad (27)$$

where  $k$  is the self-crowding factor. If mechanical interlocking takes place at the densest possible state, which is the face-centered cubic packing with  $\phi_p = 0.74$ , the apparent viscosity becomes infinitely large. Then,  $k$  takes the value of 1.35.

In this study, six simulations have been carried out with the solid volume fraction  $\phi_p = 0.0, 0.0199, 0.0503, 0.0953, 0.1414$  and  $0.1571$ . The particles are created with zero initial velocity. Again, the fluid-particle interaction is solved with a lattice resolution  $N = 20$ . The relaxation time is set to be 0.8. The number of sub-cycling and sub-cells are set to be 100 and 5, respectively. All simulations last for 14 s so that a steady state can be obtained.

#### 3.4.2. Results and discussion

Fig. 16 shows the spatial distribution of the velocity difference  $(u - u_0)$  normalized by the wall velocity  $u_w$ , where  $u$  is the calculated flow velocity averaged in the  $x$  and  $z$  directions and  $u_0$  is the theoretical linear profile for the case of pure fluid. First of all, when  $\phi_p = 0.0$ , the theoretical linear distribution of the Couette flow velocity is well

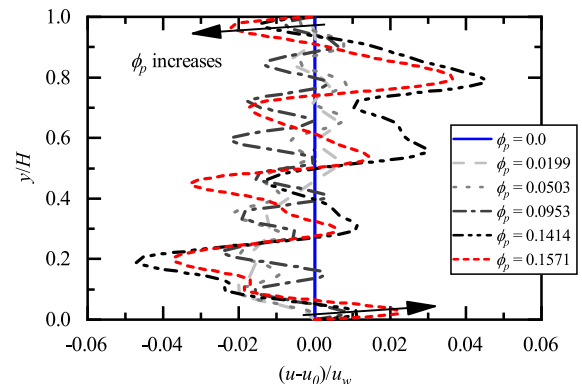


Fig. 16. Spatial distribution of the normalized velocity difference,  $(u - u_0)/u_w$ , across the planar Couette flow of suspensions with various solid volume fractions.

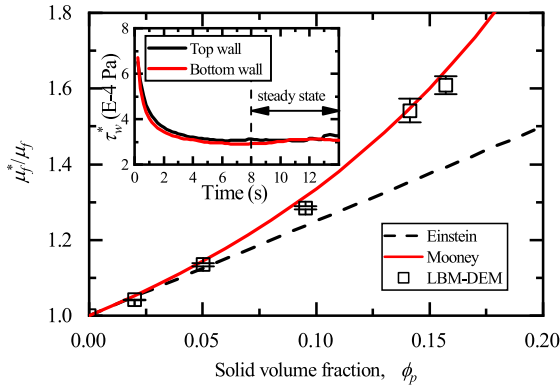


Fig. 17. Comparison between the LBM-DEM numerical results with Einstein's and Mooney's viscosity equations in terms of the relative viscosity ratio,  $\mu_f^*/\mu_f$ , at various solid volume fractions. The error bar shows the standard deviation of the numerical results. The inserted figure shows a typical evolution of the apparent shear stresses at the top and the bottom solid walls since the start of the simulation, when  $\phi_p = 0.1414$ . A steady state is reached after 8 s.

recovered by the LBM solver, which is evidenced by the zero  $(u - u_0)/u_w$  value as  $y/H$  goes from 0.0 to 1.0. As  $\phi_p$  increases, the amount of fluctuation also increases, showing a non-Newtonian behavior. Particularly, the concentrated suspension with a higher solid volume fraction  $\phi_p$  has a steeper velocity gradient close to the top and the bottom solid walls.

The strain rate at the solid boundaries are calculated from the wall velocity  $u_w$  and the flow velocity at the nearest-neighbor fluid node  $u_{\alpha,\beta}$ , see Fig. 15, where the subscripts  $\alpha$  and  $\beta$  are the spatial indices in  $x$  and  $z$  directions. Make  $n_\alpha$  and  $n_\beta$  be the number of lattice nodes in the  $x$  and  $z$  directions, respectively, the apparent wall shear stress  $\tau_w^*$  is given by:

$$\tau_w^* = \mu_f^* \dot{\gamma} = \frac{\mu_f \sum_1^{n_\alpha} \sum_1^{n_\beta} |u_w - u_{\alpha,\beta}| / \delta_x}{n_\alpha n_\beta}. \quad (28)$$

The inset of Fig. 17 shows a typical development of the apparent wall shear stresses  $\tau_w^*$  when the solid volume fraction is  $\phi_p = 0.1414$ . At the early stage, additional momentum is required to bring the stationary particles into motion. The reaction forces acting on the fluid field result in high shear stresses at the solid walls. As time goes by, the particles gradually accelerate and the wall shear stresses gradually decrease until a steady state is reached, which is about 8 s after the start of simulation. In order to calculate the apparent fluid viscosity using Eq. (28), we take the averaged wall shear stress  $\tau_w^*$  at the top and the bottom solid walls, which is further averaged over the time interval between 8 s and 14 s.

Fig. 17 shows the variation of the relative viscosity ratio,  $\mu_f^*/\mu_f$ , with the solid volume fraction. The error bar indicates the standard deviation of the LBM-DEM result due to temporal variations. Einstein's and Mooney's viscosity equations are also plotted for comparison. It can be seen that Einstein's equation only fits the data when  $\phi_p$  is roughly smaller than 0.02. While the LBM-DEM result agrees well with Mooney's equation for the whole range of  $\phi_p$  tested in this study.

### 3.5. A guideline for model setup

We would like to conclude this section by providing a simple guideline for setting up an accurate and stable LBM-DEM model to simulate an underwater granular collapse in Section 4.

First of all, it is recommended that a resolution of 20 lattice cells across one particle diameter ( $N = 20$ ) shall be used so that a highly accurate 3D LBM-DEM simulation can be achieved within the laminar and transition regimes. It is also found that the accuracy of solid ratio calculation for partially saturated cells does not have a significant effect

on the LBM-DEM results, as long as an adequate lattice resolution is used. A resolution of 5 sub-slices ( $n_{sub} = 5$ ) is high enough to offer a good estimation when the cell decomposition method is adopted.

Second, the relaxation time  $\tau$  shall be chosen depending on the Mach number. When the fluid velocity is large, the Mach number is large, a smaller  $\tau$  value is required to keep the compressibility error small. An initial relaxation time equal to 1.0 can be taken for the first trial of the LBM-DEM simulation. If the fluid density variation  $\Delta\rho_f$  is too large, simulations with smaller  $\tau$  values, larger than the lower limit 0.5, need to be conducted.

Third, the increase in  $N_{sub}$  only reduces the DEM time step, without changing the frequency of momentum exchange between the fluid and solid particles. For each predefined  $\tau$ , a large enough  $N_{sub}$  value should be adopted so that a convergent DEM solution can be achieved. After that, the particle displacement during one LBM-DEM cycle,  $\delta_p$ , should be checked so that  $\delta_p$  is small, e.g.  $\delta_p < \delta_x$  according to [26]. If  $\delta_p$  is larger than the specified criterion, the relaxation time  $\tau$  needs to be further reduced so that  $\delta_p$  gets smaller and thereby achieving a more frequent synchronization between LBM and DEM. However, a decrease in the relaxation time also comes with higher computational cost.

All in all, a successful LBM-DEM model is achieved only if the fluid flow is solved accurately with a small compressibility error (small  $\Delta\rho_f$ ) and the solid particle positions are remapped frequently (small  $\delta_p$ ). In practice, it is always suggested to conduct an additional simulation with a smaller  $\tau$  value to double check the overall convergence. Note that there exist other methods to determine the fluid and particle time steps independently according to their own stability criteria [23,25,26], which, however, may lead to very small time steps and thus unaffordable computational cost in LBM-DEM, especially for large granular packings (e.g. our immersed granular collapse problem). In this regard, we propose an approach to quickly find the most affordable time steps for LBM and DEM, which also guarantees convergence of numerical results. In fact, in immersed dense granular flows, the original stability criterion for DEM can often be relaxed because fluid-particle interactions dominate over particle-particle collisions, a conclusion made in our recent numerical study [36].

## 4. Application to immersed granular collapse

In Section 4, the guideline proposed in Section 3.5 is applied to simulate an immersed granular column collapse using LBM-DEM. The numerical results are verified against experimental data.

### 4.1. Laboratory and model configurations

In the laboratory test, glass beads (GBs) are placed behind a gate in a  $50 \times 30 \times 20$  cm transparent Perspex tank. The GBs have a mean diameter  $d_p = 1.436$  mm with a weak polydispersity of 10% standard deviation following a Gaussian distribution. The density is measured to be  $2468$  kg/m<sup>3</sup>. To initiate the granular column collapse, the gate is rapidly lifted up by a pulley system. The evolution of granular flow is videotaped by a camera of resolution 1920 by 1080 pixels at 30 frames per second so that the free surface and the runout distance can be extracted with time.

In LBM-DEM, the simulation domain is reduced to  $10 \times 5 \times 1.5$  cm to save computational time. The reduced domain is considered large enough as periodic boundaries are set in the  $z$ -direction with  $l_z = 1.5$  cm  $> 10d_p$ , so that the finite size effect is negligible. The size of DEM particles match with the GBs used in the companion experiment. Fig. 18 shows the comparison between the experiment and the numerical model in terms of the particle size distribution (PSD) curves. It can be seen that the three PSD curves of GBs determined by the QICPIC (Sympatec GmbH) analysis almost overlap with each other, showing a consistent statistical result. Besides, the PSD of the DEM particles follows the GBs quite well, with only a slightly higher percentage at around  $d_p = 1.2$  mm.

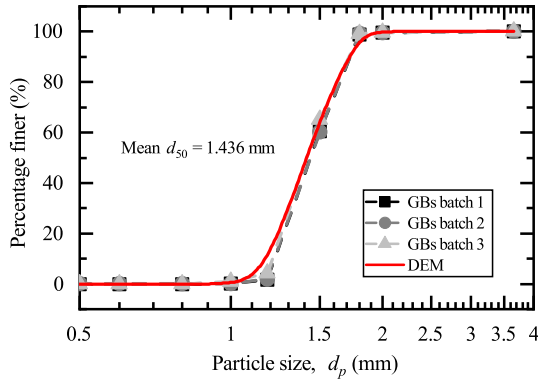


**Fig. 18.** The dashed lines with symbols show the PSD curves of three individual batches of glass beads used in the experiment, which is determined by the QICPIC analysis. The solid line without symbol shows the PSD curve of the DEM particles in the simulation.

The granular column in LBM-DEM is prepared via the following steps. First, particles with a reduced initial diameter (mean equal to  $0.5d_p$ ) are created in a space behind the gate placed at  $x = L_i = 3$  cm. The initial particle velocity is zero, and there is no initial contact. All particles are then gradually enlarged until the mean size  $d_p$  is achieved. Second, a reduced gravitational acceleration  $g(\rho_p - \rho_f)/\rho_p$ , with  $g = 9.81$  m/s<sup>2</sup>, is applied to make particles settle under water. During this sedimentation stage, the friction coefficient  $\mu$  is set to be 0.0 to achieve a dense packing. Third, once all particles are well settled down and concentrated at the lower part of the simulation domain, the friction coefficient  $\mu$  is adjusted to 0.4. Additional DEM cycles are performed until the total kinetic energy of the particles is negligible. After that, the particles located above  $y = H_i = 3.14$  cm are deleted so that a granular column with an initial aspect ratio equal to  $H_i/L_i = 1.05$  is obtained. Again, the granular systems are cycled to an equilibrium state. Finally, the linear and angular velocities of all particles are set to zero. The initial condition of the granular column can be seen in Fig. 19(a). The simulation lasts for 0.8 s of physical time at which particles almost stop moving with the overall particle kinetic energy  $E_k < 2.5 \times 10^{-10}$  J. Fig. 19(b) shows the final deposit of the granular particles at the end of the simulation.

In the experiment, an 80 Cw grit size sandpaper is glued to the bottom wall to make the base rough. Correspondingly, a layer of particles with a uniform size equal to 1 mm is glued at the bottom to mimic the basal roughness in the simulation [58]. The basal particles follow a simple cubic arrangement. All DEM particles have the same density as the GBs, i.e.,  $\rho_p = 2468$  kg/m<sup>3</sup>. For particle–particle and particle–wall

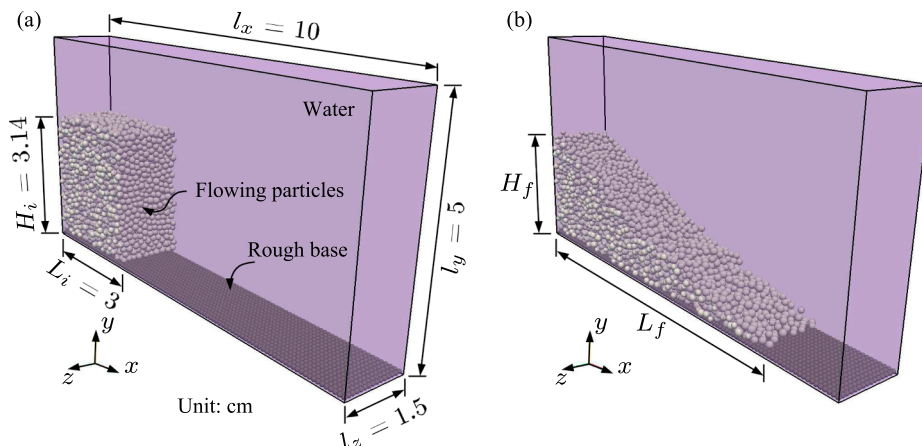


**Fig. 19.** Model configuration of a granular column collapsing in water: (a) initial condition; (b) final deposition ( $H_i$ ,  $L_i$ : initial height and length of the granular column;  $l_x$ ,  $l_y$ ,  $l_z$ : length, height and width of the simulation domain;  $H_f$ ,  $L_f$ : final height and length of the granular column).

**Table 3**

Model parameters used in 3D LBM-DEM simulation of a granular column collapse in water.

	Parameters	Values
Particle	Diameter, $d_p$	Polydisperse flowing particles: 1.436 mm $\pm$ 10% Monodisperse fixed basal particles: 1.0 mm
	Density, $\rho_p$	2468 kg/m <sup>3</sup>
	Young's modulus, $E$	$10^9$ Pa
	Poisson's ratio, $\nu$	0.24
	Coefficient of restitution, $e$	0.65
	Coefficient of friction, $\mu$	0.4
Fluid	Density, $\rho_f$	1000 kg/m <sup>3</sup>
	Dynamic viscosity, $\mu_f$	0.001 Pa s
Simulation box	Length, $l_x$	0.1 m
	Height, $l_y$	0.05 m
	Width, $l_z$	0.015 m
Resolution	DEM time step, $\Delta t$	$5.16 \cdot 10^{-8}$ s
	LBM time step, $\delta_t$	$5.16 \cdot 10^{-6}$ s
	Lattice spacing, $\delta_x$	0.0718 mm

collisions, a Young's modulus and a Poisson's ratio equal to  $10^9$  Pa and 0.24, respectively, are adopted. The coefficient of restitution is 0.65, according to the property of glass. The granular column is fully immersed in water with density  $\rho_f = 1000$  kg/m<sup>3</sup> and dynamic viscosity  $\mu_f = 0.001$  Pa s. The top surface is set to be a free-slip boundary condition, while no-slip boundary conditions are defined for the bottom wall, and the side walls facing the x-direction.

Other model parameters involved in the LBM-DEM algorithm can be chosen following the guideline provided in Section 3.5. The spatial resolution and the number of sub-cells are specified as  $N = 20$  and  $n_{sub} = 5$ , respectively. The relaxation time is selected to be  $\tau = 0.503$ , resulting in the LBM time step  $\delta_t = 5.16 \cdot 10^{-6}$  s. Following Eq. (17) with  $N_{sub} = 100$ , the calculated DEM time step is  $\Delta t = 5.16 \cdot 10^{-8}$  s. Table 3 summarizes the key model parameters.

#### 4.2. Collapse dynamics and runoff

The free-surface of the GBs in the experiment can be automatically detected according to the contrast in brightness using the MATLAB image processing toolbox (the GBs are brighter while the background

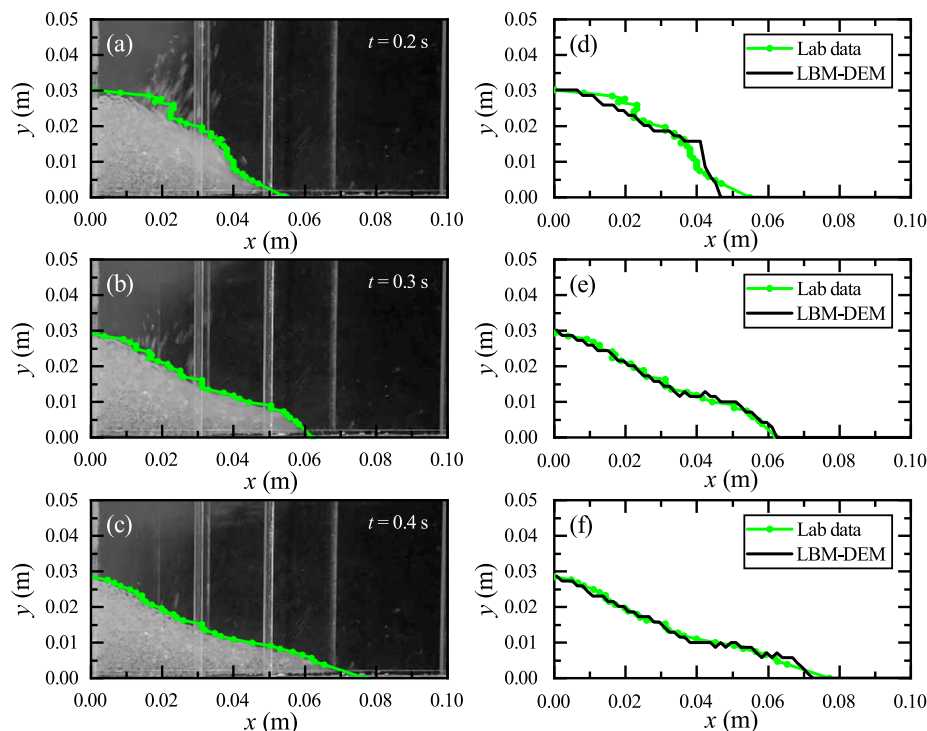


**Fig. 20.** (a–c) Snapshots of the immersed granular column collapse in the experiments at  $t = 0.2$  s,  $0.3$  s, and  $0.4$  s, respectively. The green lines depict the free-surface of the granular flow; (d–f) comparison of the granular flow free-surface between the experiment and the LBM-DEM simulation at  $t = 0.2$  s,  $0.3$  s, and  $0.4$  s, respectively.

fluid field is much darker), as shown in Fig. 20(a)–(c) at  $t = 0.2$  s,  $0.3$  s and  $0.4$  s. In the numerical simulation, the interface between the DEM particles and the water can be determined by a cut-off local porosity equal to 0.8, above which we consider as pure water. Fig. 20(d)–(f) compare the experimental data and the numerical results in terms of the free surface of the granular phase at  $t = 0.2$  s,  $0.3$  s and  $0.4$  s. Excellent agreement is achieved. The small discrepancy at the early stage ( $t = 0.2$  s) is attributed to the gate removal effect in the experiment, which is not simulated in the numerical model.

The front positions of the GBs and the DEM particles are determined from the free-surface profiles and normalized by the initial length  $L_i$ , which are compared in Fig. 21. There are fluctuations observed for the experimental data mainly because the brightness contrast at the surge front of the GBs is relatively low, for example, in Fig. 20(c), making it difficult to determine the exact position of the surge front. Apart from this, the numerical results agree with the experimental data very well. By explicitly setting the model parameters according to the guideline in Section 3.5, we can easily capture the complex dynamics of the immersed granular column collapse accurately, without much effort in tuning the parameters.

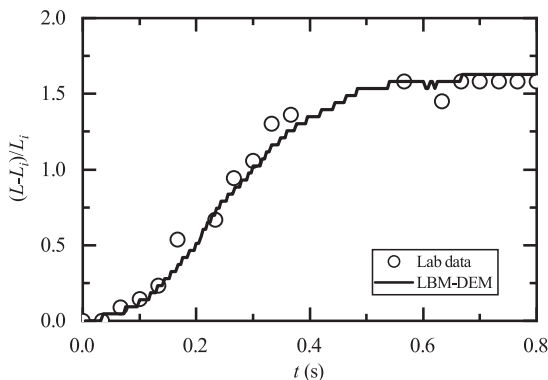


**Fig. 21.** Comparison of the normalized front position,  $(L - L_i)/L_i$ , between the experimental data and the numerical results.

## 5. Concluding remarks

This study presents a numerical simulation of the dense granular shear flows immersed in a viscous fluid. A 3D coupled LBM-DEM method is adopted, in which the particle motion in a granular system is solved by DEM, while LBM is applied to solve the hydrodynamics of fluid flows. The interaction between DEM particles and the LBM fluid is achieved by an immersed moving boundary technique, based on the conservation of momentum. Different from CFD-DEM and continuum methods based on the mixture theory, the presented LBM-DEM model is able to explicitly resolve the pore-scale fluid flow and the complex fluid-particle interactions in an efficient manner. The following conclusions are drawn:

- To capture the transient dynamics of an immersed granular collapse, the LBM-DEM model is first validated against four benchmark cases. A parametric study is carried out to examine various sources of numerical errors. It is found that at least 20 lattice cells per one particle diameter shall be used so that the errors in viscous drag and torque are below 5%. A small relaxation time greater than the lower limit 0.5 shall be used to ensure a small fluid compressibility error and to strengthen the degree of coupling between fluid and particles if the computational cost is affordable. As long as the fluid-particle interaction is resolved adequately in space and time (high  $N$  and small  $\tau$ ), the lubrication effects can be well captured benefiting from the SGS resolution of the IMB method, without the need of an artificial lubrication model for immersed dense shear flows.
- A guideline is proposed to quickly establish a LBM-DEM model for immersed granular collapses with high accuracy, stability and efficiency. More efforts might be required to further extend the guideline to more specific applications, for example, particles travelling in turbulent flows and erosion of well graded soils.
- Following the proposed guideline, the LBM-DEM method is applied to simulate a granular column collapse in water. A companion experiment is also carried out for comparison. It is found that the LBM-DEM model can successfully capture the collapse dynamics, which highlights the potential of using the LBM-DEM method to study the pore-scale physics involved in large-scale geophysical flows.

With the current computational power, the use of LBM-DEM is still limited to simulations with a modest number of particles. To directly simulate large-scale geophysical flows, one of the available options is to adopt a continuum approach. In this regard, LBM-DEM can be a handy tool to derive rheological models that can be incorporated into the continuum framework to bridge micro and macro scales.

## Acknowledgements

This research is conducted in part using the research computing facilities and/or advisory services offered by Information Technology Services, the University of Hong Kong and under the support of FAP-DF, Brazil.

## References

- Iverson RM, Reid ME, Iverson NR, LaHusen RG, Logan M, Mann JE, et al. Acute sensitivity of landslide rates to initial soil porosity. *Science* 2000;290(5491):513–6. <https://doi.org/10.1126/science.290.5491.513>.
- Whitaker S. Flow in porous media. I: A theoretical derivation of Darcy's law. *Transport Porous Media* 1986;1(1):3–25. <https://doi.org/10.1007/bf01036523>.
- Ergun S. Fluid flow through packed columns. *Chem Eng Prog* 1952;48:89–94.
- Macdonald IF, El-Sayed MS, Mow K, Dullien FAL. Flow through porous media—the ergun equation revisited. *Ind Eng Chem Fund* 1979;18(3):199–208. <https://doi.org/10.1021/i160071a001>.
- Jing L, Kwok CY, Leung YF, Sobral YD. Extended CFD–DEM for free-surface flow with multi-size granules. *Int J Numer Anal Meth Geomech* 2016;40(1):62–79. <https://doi.org/10.1002/nag.2387>.
- Zhao J, Shan T. Coupled CFD–DEM simulation of fluid-particle interaction in geomechanics. *Powder Technol* 2013;239:248–58. <https://doi.org/10.1016/j.powtec.2013.02.003>.
- Kloss C, Goniva C, Hager A, Amberger S, Pirker S. Models, algorithms and validation for open-source DEM and CFD-DEM. *Prog Comput Fluid Dyn Int J* 2012;12(2–3):140–52. <https://doi.org/10.1504/pcfd.2012.047457>.
- Jing L, Yang GC, Kwok CY, Sobral YD. Dynamics and scaling laws of underwater granular collapse with varying aspect ratios. *Phys Rev E* 2018;98(4). <https://doi.org/10.1103/PhysRevE.98.042901>.
- Kim J, Kim D, Choi H. An immersed-boundary finite-volume method for simulations of flow in complex geometries. *J Comput Phys* 2001;171(1):132–50. <https://doi.org/10.1006/jcph.2001.6778>.
- Peskin CS. The immersed boundary method. *Acta Numer* 2002;11:479–517. <https://doi.org/10.1017/S0962492902000077>.
- Hager A, Kloss C, Pirker S, Goniva C. Parallel open source CFD-DEM for resolved particle-fluid interaction. *J Energy Power Eng* 2013;7(9):1705.
- Qian YH, Humières DD, Lallemand P. Lattice BGK models for Navier-Stokes equation. *Europhys Lett* 1992;17(6):479.
- Chen S, Doolen GD. Lattice Boltzmann method for fluid flows. *Ann Rev Fluid Mech* 1998;30(1):329–64. <https://doi.org/10.1146/annurev.fluid.30.1.329>.
- Yang GC, Kwok CY, Sobral YD. The effects of bed form roughness on total suspended load via the Lattice Boltzmann Method. *Appl Math Model* 2018;63:591–610. <https://doi.org/10.1016/j.apm.2018.07.011>.
- Ladd AJC. Numerical simulations of particulate suspensions via a discretized Boltzmann equation. Part I. Theoretical foundation. *J Fluid Mech* 1994;271:285–309. <https://doi.org/10.1017/S0022112094001771>.
- Aidun CK, Lu Y, Ding EJ. Direct analysis of particulate suspensions with inertia using the discrete Boltzmann equation. *J Fluid Mech* 1998;373:287–311. <https://doi.org/10.1017/S0022112098002493>.
- Noble DR, Torczynski JR. A Lattice-Boltzmann method for partially saturated computational cells. *Int J Modern Phys C* 1998;09(08):1189–201. <https://doi.org/10.1142/s0129183198001084>.
- Holdych DJ. Lattice Boltzmann methods for diffuse and mobile interfaces, vol. 64–03. ProQuest Dissertations And Theses; 2003.
- Han Y, Cundall PA. Resolution sensitivity of momentum-exchange and immersed boundary methods for solid-fluid interaction in the lattice Boltzmann method. *Int J Numer Meth Fluids* 2011;67(3):314–27. <https://doi.org/10.1002/flid.2353>.
- Rettinger C, Rude U. A comparative study of fluid-particle coupling methods for fully resolved lattice Boltzmann simulations. *Comput Fluids* 2017;154:74–89. <https://doi.org/10.1016/j.compfluid.2017.05.033>.
- Kutay ME, Aydılek AH, Masad E. Laboratory validation of lattice Boltzmann method for modeling pore-scale flow in granular materials. *Comput Geotech* 2006;33(8):381–95. <https://doi.org/10.1016/j.compgeo.2006.08.002>.
- Han K, Feng YT, Owen DRJ. Numerical simulations of irregular particle transport in turbulent flows using coupled LBM-DEM. *Comput Model Eng Sci* 2007;18(2):87.
- Feng YT, Han K, Owen DRJ. Coupled lattice Boltzmann method and discrete element modelling of particle transport in turbulent fluid flows: computational issues. *Int J Numer Meth Eng* 2007;72(9):1111–34. <https://doi.org/10.1002/nme.2114>.
- Strack OE, Cook BK. Three-dimensional immersed boundary conditions for moving solids in the lattice-Boltzmann method. *Int J Numer Meth Fluids* 2007;55(2):103–25. <https://doi.org/10.1002/flid.1437>.
- Feng YT, Han K, Owen DRJ. Combined three-dimensional lattice Boltzmann method and discrete element method for modelling fluid-particle interactions with experimental assessment. *Int J Numer Meth Eng* 2010;81(2):229–45. <https://doi.org/10.1002/nme.2689>.
- Owen DRJ, Leonardi CR, Feng YT. An efficient framework for fluid-structure interaction using the lattice Boltzmann method and immersed moving boundaries. *Int J Numer Meth Eng* 2011;87(1–5):66–95. <https://doi.org/10.1002/nme.2985>.
- Lominé F, Scholtès L, Sibille L, Poullain P. Modeling of fluid-solid interaction in granular media with coupled lattice Boltzmann/discrete element methods: application to piping erosion. *Int J Numer Anal Meth Geomech* 2013;37(6):577–96. <https://doi.org/10.1002/nag.1109>.
- Han Y, Cundall PA. LBM-DEM modeling of fluid-solid interaction in porous media. *Int J Numer Anal Meth Geomech* 2013;37(10):1391–407. <https://doi.org/10.1002/nag.2096>.
- Wang M, Feng YT, Pande GN, Chan AHC, Zuo WX. Numerical modelling of fluid-induced soil erosion in granular filters using a coupled bonded particle lattice Boltzmann method. *Comput Geotech* 2017;82:134–43. <https://doi.org/10.1016/j.compgeo.2016.10.006>.
- Wang M, Feng Y, Pande G, Zhao T. A coupled 3-dimensional bonded discrete element and lattice Boltzmann method for fluid-solid coupling in cohesive geomaterials. *Int J Numer Anal Meth Geomech* 2018;42(12):1405–24. <https://doi.org/10.1002/nag.2799>.
- Rondon L, Pouliquen O, Aussillous P. Granular collapse in a fluid: role of the initial volume fraction. *Phys Fluids* 2011;23(7). <https://doi.org/10.1063/1.3594200.073301>.
- Rettinger C, Rude U. A coupled lattice Boltzmann method and discrete element method for discrete particle simulations of particulate flows. *Comput Fluids* 2018;172:706–19. <https://doi.org/10.1016/j.compfluid.2018.01.023>.
- Topin V, Monerie Y, Perales F, Radjai F. Collapse dynamics and runoff of dense granular materials in a fluid. *Phys Rev Lett* 2012;109(18). 188001.
- ten Cate A, Nieuwstad CH, Derksen JJ, Akker HEAVD. Particle imaging velocimetry experiments and lattice-Boltzmann simulations on a single sphere settling under gravity. *Phys Fluids* 2002;14(11):4012–25. <https://doi.org/10.1063/1.1512918>.
- Wang C, Wang Y, Peng C, Meng X. Dilatancy and compaction effects on the submerged granular column collapse. *Phys Fluids* 2017;29(10). <https://doi.org/10.1063/1.4986502>. 103307.
- Jing L, Yang GC, Kwok CY, Sobral YD. Flow regimes and dynamic similarity of immersed granular collapse: a cfd-dem investigation. *Powder Technol*. doi:<https://doi.org/10.1016/j.powtec.2019.01.029>.
- Mei R, Shyy W, Yu D, Luo LS. Lattice Boltzmann method for 3-D flows with curved boundary. *J Comput Phys* 2000;161(2):680–99. <https://doi.org/10.1006/jcph.2000.6522>.
- Bhatnagar PL, Gross EP, Krook M. A model for collision processes in gases. I. Small amplitude processes in charged and neutral one-component systems. *Phys Rev* 1954;94(3):511–25.
- Aidun CK, Clausen JR. Lattice-Boltzmann for complex flows. *Ann Rev Fluid Mech* 2010;42(1):439–72. <https://doi.org/10.1146/annurev-fluid-121108-145519>.
- He X, Luo LS. Lattice Boltzmann model for the incompressible Navier-Stokes equation. *J Stat Phys* 1997;88(3):927–44. <https://doi.org/10.1023/B:JOSS.0000015179.12689.e4>.
- Davis RH, Serayssol J-M, Hinch EJ. The elasto-hydrodynamic collision of two spheres. *J Fluid Mech* 1986;163:479–97. <https://doi.org/10.1017/S0022112086002392>.
- Cundall PA, Strack OD. A discrete numerical model for granular assemblies. *Geotechnique* 1979;29(1):47–65.
- Di Renzo A, Di Maio FP. Comparison of contact-force models for the simulation of collisions in DEM-based granular flow codes. *Chem Eng Sci* 2004;59(3):525–41. <https://doi.org/10.1016/j.ces.2003.09.037>.
- Verlet L. Computer “experiments” on classical fluids. I. Thermodynamical properties of Lennard-Jones molecules. *Phys Rev* 1967;159(1):98–103. <https://doi.org/10.1103/PhysRev.159.98>.
- Wang M, Feng YT, Owen DRJ, Qu TM. A novel algorithm of immersed moving boundary scheme for fluid-particle interactions in DEM-LBM. *Comput Meth Appl Mech Eng* 2019;346:109–25. <https://doi.org/10.1016/j.cma.2018.12.001>.
- Zou Q, He X. On pressure and velocity boundary conditions for the lattice Boltzmann BGK model. *Phys Fluids* 1997;9(6):1591–8. <https://doi.org/10.1063/1.869307>.
- Seil P, Pirker S. LBDEM coupling: open-source power for fluid-particle systems. In: Proceedings of the 7th international conference on discrete element methods. Springer. p. 679–86. doi: [10.1007/978-981-10-1926-5\\_70](https://doi.org/10.1007/978-981-10-1926-5_70).
- Catherine O, Bray JD. Selecting a suitable time step for discrete element simulations that use the central difference time integration scheme. *Eng Comput* 2004;21(2/3/4):278–303. <https://doi.org/10.1108/02644400410519794>.
- Happel J, Brenner H. Low Reynolds number hydrodynamics: with special applications to particulate media vol. 1. Springer Science & Business Media; 1983. <https://www.springer.com/gp/book/9789024728770>.
- Clague DS, Cornelius PJ. The hydrodynamic force and torque on a bounded sphere in Poiseuille flow. *Int J Numer Meth Fluids* 2001;35(1):55–70. [https://doi.org/10.1002/1097-0363\(20010115\)35:1<55::AID-FLD83>3.0.CO;2-W](https://doi.org/10.1002/1097-0363(20010115)35:1<55::AID-FLD83>3.0.CO;2-W).
- Luo L-S, Liao W, Chen X, Peng Y, Zhang W. Numerics of the lattice Boltzmann method: effects of collision models on the lattice Boltzmann simulations. *Phys Rev E* 2011;83(5). 056710.
- Wang D, Leonardi CR, Aminossadati SM. Improved coupling of time integration and hydrodynamic interaction in particle suspensions using the lattice Boltzmann and discrete element methods. *Comput Math Appl* 2018;75(7):2593–606. <https://doi.org/10.1016/j.camwa.2018.01.002>.
- Cheng C, Galindo-Torres SA, Zhang X, Zhang P, Scheuermann A, Li L. An improved immersed moving boundary for the coupled discrete element lattice Boltzmann

- method. *Comput Fluids* 2018;177:12–9. <https://doi.org/10.1016/j.compfluid.2018.09.018>.
- [54] Batchelor GK. *An introduction to fluid dynamics*. Cambridge: Mathematical Library, Cambridge University Press; 2000. <https://doi.org/10.1017/CBO9780511800955>.
- [55] Niven RK. Physical insight into the ergun and Wen & Yu equations for fluid flow in packed and fluidised beds. *Chem Eng Sci* 2002;57(3):527–34. [https://doi.org/10.1016/S0009-2509\(01\)00371-2](https://doi.org/10.1016/S0009-2509(01)00371-2).
- [56] Hou S, Sterling J, Chen S, Doolen GD. A lattice Boltzmann sub-grid model for high Reynolds number flows. *Pattern Form Latt Gas Autom* 1996;6:149. arXiv:comp-gas/9401004.
- [57] Mooney M. The viscosity of a concentrated suspension of spherical particles. *J Colloid Sci* 1951;6(2):162–70.
- [58] Jing L, Kwok CY, Leung YF, Sobral YD. Characterization of base roughness for granular chute flows. *Phys Rev E* 2016;94(5). <https://doi.org/10.1103/PhysRevE.94.052901>. 052901.